Triple oxygen isotope constraints on atmospheric O_2 and biological productivity during the mid-Proterozoic

Peng Liu[a,b,c,1,2], Jingjun Liu[b,d,1], Aoshuang Ji[b], Christopher T. Reinhard[e,f], Noah J. Planavsky[d,f], Dmitri Babikov[g], Raymond G. Najjar[h], and James F. Kasting[b,2]

[a]Frontiers Science Center for Deep Ocean Multispheres and Earth System, Key Lab of Submarine Geosciences and Prospecting Techniques, Ministry of Education and College of Marine Geosciences, Ocean University of China, Qingdao 266100, China; [b]Department of Geosciences, The Pennsylvania State University, University Park, PA 16802; [c]Department of Atmospheric and Oceanic Sciences, Peking University, Beijing 100871, China; [d]Department of Earth and Planetary Sciences, Yale University, New Haven, CT 06511; [e]School of Earth and Atmospheric Sciences, Georgia Institute of Technology, Atlanta, GA 30332; [f]Alternative Earths Team, NASA Interdisciplinary Consortia for Astrobiology Research, Riverside, CA 92521; [g]Department of Chemistry, Marquette University, Milwaukee, WI 53201; and [h]Department of Meteorology and Atmospheric Science, The Pennsylvania State University, University Park, PA 16802

Edited by Mark Thiemens, University of California San Diego, La Jolla, CA; received March 17, 2021; accepted November 2, 2021

Reconstructing the history of biological productivity and atmospheric oxygen partial pressure (pO_2) is a fundamental goal of geobiology. Recently, the mass-independent fractionation of oxygen isotopes (O-MIF) has been used as a tool for estimating pO_2 and productivity during the Proterozoic. O-MIF, reported as $\Delta'^{17}O$, is produced during the formation of ozone and destroyed by isotopic exchange with water by biological and chemical processes. Atmospheric O-MIF can be preserved in the geologic record when pyrite (FeS_2) is oxidized during weathering, and the sulfur is redeposited as sulfate. Here, sedimentary sulfates from the ∼1.4-Ga Sibley Formation are reanalyzed using a detailed one-dimensional photochemical model that includes physical constraints on air–sea gas exchange. Previous analyses of these data concluded that pO_2 at that time was <1% PAL (times the present atmospheric level). Our model shows that the upper limit on pO_2 is essentially unconstrained by these data. Indeed, pO_2 levels below 0.8% PAL are possible only if atmospheric methane was more abundant than today (so that pCO_2 could have been lower) or if the Sibley O-MIF data were diluted by reprocessing before the sulfates were deposited. Our model also shows that, contrary to previous assertions, marine productivity cannot be reliably constrained by the O-MIF data because the exchange of molecular oxygen (O_2) between the atmosphere and surface ocean is controlled more by air–sea gas transfer rates than by biological productivity. Improved estimates of pCO_2 and/or improved proxies for $\Delta'^{17}O$ of atmospheric O_2 would allow tighter constraints to be placed on mid-Proterozoic pO_2.

mass-independent isotope fractionation | atmospheric O_2 | mid-Proterozoic | biological productivity | gross primary productivity

The oxygenation of Earth's atmosphere–ocean system is widely considered to have occurred through two major step function increases in atmospheric oxygen (O_2) (1, 2). In the first of these steps, referred to as the "Great Oxidation Event," Earth's atmosphere transitioned from a weakly reducing state in which O_2 was poorly mixed and vanishingly low in abundance (3, 4) to a state in which atmospheric O_2 was present in sufficient abundance to prevent the production and transfer of mass-independent fractionation (MIF) of sulfur isotopes to marine sediments (5). Photochemical models indicate that the disappearance of these signals from the rock record at ∼2.3 billion years ago (Ga) (6) requires atmospheric O_2 levels above $\sim 10^{-5}$ times the present atmospheric level (PAL) (7). A second increase in ocean–atmosphere O_2 levels is now considered to have occurred at some time between ∼800 to 400 Ma, during which time atmospheric O_2 began to approach roughly modern values, and the ocean interior became periodically and then more or less permanently well oxygenated (2, 8, 9).

However, atmospheric O_2 levels in between these two broad steps in Earth system oxygenation remain debated and poorly constrained. Evidence for widespread anoxia in the ocean interior has been taken to suggest atmospheric O_2 levels below ∼40% PAL (1, 10). Estimates based on stable chromium (Cr) isotopes in shales and oolitic ironstones (11, 12), cerium (Ce) systematics in marine carbonates (13, 14), and iron (Fe) retention patterns in ancient soil horizons (15) are all consistent with very low atmospheric O_2, perhaps below ∼1% PAL. In contrast, trace element abundances and isotopic signatures in shales (16–18) and iodine systematics of marine carbonate concretions (19) have been used to suggest higher atmospheric O_2 levels, well above ∼1% PAL and perhaps even >10% PAL. A reanalysis of the Ce anomaly data also suggests atmospheric oxygen partial pressure (pO_2) > 1% PAL (20). Constraining atmospheric O_2 prior to the emergence and ecological expansion of metazoan (animal) life is essential for understanding the relative roles of intrinsic biological factors and environmental

Significance

Constraining the abundance of molecular oxygen (O_2) in Earth's atmosphere over time is a problem of central importance for understanding the evolution of complex life. Here, we refine previous analyses of the rare oxygen isotope composition of sedimentary sulfates to develop improved estimates of atmospheric O_2 during Earth's mid-Proterozoic era. Previous analyses of these data had predicted O_2 concentrations well below 1% present atmospheric level. Our new calculations suggest that this value is closer to a lower limit on atmospheric oxygen partial pressure unless the climate was warmed significantly by biogenic methane. The calculations also show that marine productivity cannot be reliably estimated from these data because of the slow rate of transfer of O_2 across the air–sea interface.

Author contributions: P.L., J.L., A.J., C.T.R., N.J.P., D.B., R.G.N., and J.F.K. designed research; P.L., J.L. and J.F.K. performed research; P.L., J.L., D.B., and J.F.K. contributed new reagents/analytic tools; P.L., J.L., A.J., C.T.R., N.J.P., D.B., R.G.N., and J.F.K. analyzed data; and P.L., J.L., A.J., C.T.R., N.J.P., D.B., R.G.N., and J.F.K. wrote the paper.

The authors declare no competing interest.

This article is a PNAS Direct Submission.

[1]P.L. and J.L. contributed equally to this work.

[2]To whom correspondence may be addressed. Email: pxl97@psu.edu or jfk4@psu.edu.

This article contains supporting information online at http://www.pnas.org/lookup/suppl/doi:10.1073/pnas.2105074118/-/DCSupplemental.

Published December 15, 2021.

drivers (or, more likely, their interplay) in controlling the expansion of biological complexity and, in particular, the rise of animals (21–23). Understanding how primary productivity has changed through time as atmospheric O_2 rose is also a fundamental unanswered question about Earth's history (e.g., refs. 24 to 26).

Here, we employ a tool for estimating ancient pO_2 and primary productivity in deep time: the triple oxygen isotope composition of marine and lacustrine sedimentary rocks. This approach utilizes oxygen isotope signatures that deviate significantly from the usual mass-dependent fractionation (MDF) line. Today, about 30% of this oxygen MIF (O-MIF) signal originates from ozone (O_3) photochemistry, and we expect that this percentage was considerably higher in the past (*SI Appendix*, section 1.2). The O-MIF value can be defined by the relationship (27)

$$\frac{\Delta'^{17}O}{1000} \equiv \ln\left(\frac{\delta^{17}O}{1000}+1\right) - \lambda_{RL}\cdot\ln\left(\frac{\delta^{18}O}{1000}+1\right). \quad [1]$$

Here, $\delta^{x}O$ represents the deviation in parts per thousand (‰, or "permil") from the $^{x}O/^{16}O$ ratio in an isotopic standard, and λ_{RL} is a reference line slope that we take to be equal to 0.528, following Young et al. (28) and Pack (27). For small fractionations, this reduces to

$$\Delta^{17}O \cong \delta^{17}O - \lambda_{RL}\cdot\delta^{18}O. \quad [2]$$

We use the logarithmic form (Eq. **1**) in all calculations, as the fractionation in ozone is not small. The positive $\Delta'^{17}O$ signal from ozone (~26‰ at the surface) is transferred to CO_2, and O_2 acquires a negative $\Delta'^{17}O$ signal (~−0.43‰ at the surface) by mass balance (27). The $\Delta'^{17}O$ signal from atmospheric O_2 can be transferred to the rock record via weathering of pyrite, FeS_2, and the subsequent burial of oxidized sulfur phases at Earth's surface (25, 29, 30). Some authors have recently suggested that H_2O_2 may be responsible for oxidizing pyrite in rivers draining the Himalayas (31), so we keep track of $\Delta'^{17}O$ of H_2O_2 as well. Small changes in $\Delta'^{17}O$ can also be induced by mass-dependent processes with different values for λ_{RL} as discussed further below (see the section *Dilution of the O-MIF Signal in O_2 and CO_2 via Biospheric Recycling*). We use the term "O-MIF" only to refer to the large changes induced by ozone formation.

On the present Earth, $\Delta'^{17}O$ values are small, roughly −0.05‰ in seawater sulfate (32, 33) and −0.43‰ in tropospheric O_2 (27). By comparison, the existing oxygen isotope record from sedimentary sulfate minerals deposited during the Proterozoic shows values as light as −0.9‰ (25), requiring tropospheric O_2 values significantly lighter than those of the modern atmosphere. The overall magnitude of these signals is controlled by atmospheric O_2 and CO_2, which act to control the production and storage of isotopic anomalies in the atmosphere and by the globally integrated productivity of the biosphere, which acts to eliminate MIF (34, 35). As a result, if one knows (or can assume) atmospheric pCO_2, one can either use an assumed atmospheric pO_2 to estimate global gross primary production, GPP (25, 36), or invert for an estimate of atmospheric pO_2 (15, 37). (GPP is the total rate of synthesis of fresh organic matter, which, for an aerobic ecosystem, is just the rate of oxygenic photosynthesis.) However, previous attempts to solve for pO_2 (*ibid.*) used a box modeling approach that mischaracterized the effect of stratosphere–troposphere gas exchange at low pO_2, made potentially problematic assumptions about the link between GPP and air–sea O_2 transfer, and left out other key aspects of atmospheric chemistry.

Here, we revisit this problem with a detailed one-dimensional photochemical and ocean–atmosphere gas exchange model. This approach includes several advances that allow for a more realistic representation of the oxygen cycle. First, our photochemical model explicitly calculates the lowering of the ozone layer as atmospheric O_2 decreases (38) and directly simulates the photochemically catalyzed isotopic exchange between O_2 (or O_3) and gaseous H_2O. Second, our model includes limitations imposed by gas exchange rates across the air–sea interface. At O_2 levels lower than today, the gas transfer rate, rather than GPP itself, should control the extent of biospheric recycling of $\Delta'^{17}O$ values.

Production of the O-MIF ($\Delta'^{17}O$) Signal during Ozone Formation

O-MIF in Earth's atmosphere is mainly produced by the ozone formation reaction (39–41)

$$O + O_2 + M \rightarrow O_3 + M. \quad [3]$$

Here, "O" is the ground state of atomic oxygen, and "M" represents a third molecule needed to carry off the excess energy of the collision. Ozone is a bent molecule with a resonant double bond between three oxygen atoms (*SI Appendix*, Table S6). If we let "Q" represent a minor isotope of O (i.e., ^{17}O or ^{18}O), the isotopic analogs of reaction [**3**] can be written as

$$O + OQ + M \rightarrow OOQ + M, \quad [4]$$

$$O + OQ + M \rightarrow OQO + M, \quad [5]$$

and

$$Q + O_2 + M \rightarrow OOQ + M. \quad [6]$$

Two different forms of ozone are created: asymmetric OOQ (reactions [**4**] and [**6**]) and symmetric OQO (reaction [**5**]). The rate constants for these reactions are given in *SI Appendix*, Table S2. Asymmetric ozone in reaction [**4**] forms ~16% faster than symmetric ozone in reaction [**5**] (the so-called "η effect" in the chemical physics literature (40, 42–44). This effect depends on both temperature (45) and pressure (46). Reaction [**6**] forms asymmetric ozone as well, but its rate constant is roughly equal to that of reaction [**3**] (for ^{17}O), or even slower (for ^{18}O), for reasons that are related to the rapid isotope exchange reaction

$$Q + O_2 \leftrightarrow OQ + O. \quad [7]$$

The rate of isotope exchange as well as the rate of ozone formation is influenced by the symmetry number of two for the O_2 molecule and by the vibrational zero-point energy difference between lighter OO and heavier OQ. The net result is that O_3 becomes enriched in minor isotopes (Q atoms) by about 70‰ (^{17}O) and 75‰ (^{18}O), producing $\Delta'^{17}O$ values of ~30‰ following Eq. **1**. This large enrichment has been confirmed by stratospheric observations made from balloon flights (47–49). The enrichment is then transferred to CO_2 via the reaction sequences (50)

$$OOQ + h\nu \rightarrow O_2 + Q(^1D) \quad [8]$$

and

$$Q(^1D) + CO_2 \rightarrow COQ + O. \quad [9]$$

Here, $h\nu$ represents an ultraviolet photon, and $Q(^1D)$ is an excited electronic state of atomic oxygen. Thus, atmospheric CO_2 acquires positive $\Delta'^{17}O$ inherited from ozone. The excess Q atoms in CO_2 are ultimately derived from O_2; hence, O_2 acquires negative $\Delta'^{17}O$. However, because O_2 is ~500 times more abundant than CO_2 in the modern atmosphere, the negative $\Delta'^{17}O$ values in O_2 are much smaller than the positive $\Delta'^{17}O$ values in CO_2. $Q(^1D)$ can also react with other species (e.g., H_2O and CH_4), thereby spreading the O-MIF signal throughout the photochemical network.

Dilution of the O-MIF Signal in O_2 and CO_2 via Biospheric Recycling

Recycling by the Marine Biosphere. The O-MIF signal in O_2 and CO_2 can be diluted by processing through the terrestrial and marine biospheres (35). Consider the marine biosphere first. CO_2 dissociates in solution to form carbonic acid and other forms of dissolved inorganic carbon (DIC), all of which readily exchange O atoms with water. [The time scale for isotopic exchange is essentially equal to the time scale for CO_2 hydration, which is of the order of minutes (51). By comparison, the residence time of CO_2 in the surface ocean is ~20 d, as shown in *SI Appendix*, section 2.1.2. (CO_2 and O_2 behave similarly because their air-sea transfer veocities are nearly the same.) Thus, whenever CO_2 dissolves in water, it loses its O-MIF signal. However, the situation is quite different for O_2. Dissolved oxygen does not exchange O atoms with water unless it is used for respiration (35), which can be represented by reaction [**10**] running to the right

$$CH_2O + O_2 \leftrightarrow CO_2 + H_2O. \quad [10]$$

The reverse of respiration is photosynthesis, which is represented by reaction [**10**] running to the left.

Respiration dilutes the O-MIF signal in O_2 by reducing much of it to water and adding some O atoms to other molecules. However, it also creates a small $\Delta'^{17}O$ signal by way of a phenomenon called the "Dole effect." Respiration induces strong MDF because lighter O isotopes are taken up faster than heavier ones (52). This causes atmospheric O_2 to be enriched in minor isotopes by ~23.5‰ for ^{18}O and ~12‰ for ^{17}O (28). The slope of the MDF line for respiration is ~0.515 (28), which is slightly lower than the slope of the normal terrestrial MDF line given by Eq. **1**. This difference imparts a negative $\Delta'^{17}O$ signal to O_2, which is important when we compare our model to observed values in *Fits to Modern Earth*. This process is less of a complication at low pO_2 levels because air–sea gas transfer rates decrease while the O-MIF in O_2 signal becomes substantially larger; hence, we have elected to ignore it in our low-O_2 calculations. We justify this assumption explicitly in *SI Appendix*, section 1.2.

The processing of the O-MIF signal by the marine biosphere is complicated because air–sea gas transfer limitations also play a role. The net downward flux of gas X across the atmosphere–ocean interface can be expressed as a "piston velocity," k_X, times a concentration difference over a thin boundary layer at the ocean's surface:

$$\Phi(X) = k_X \cdot \{\alpha_X \cdot pX - [X_{aq}]\}. \quad [11]$$

The piston velocity can be related to the product of the 10-m average wind speed and the Schmidt number of the fluid (53) (*SI Appendix*, section 2.1.2). The remaining terms in Eq. **11** are the Henry's Law coefficient α_x and the species atmospheric partial pressure pX. $[X_{aq}]$ is the dissolved concentration of the gas in the surface ocean. We found that, $k_{O_2} \cong 5.0$ m · d^{-1}, and $k_{CO_2} \cong 4.7$ m · d^{-1}.

Note that $\Phi(X)$ in Eq. **11** is a net flux, the difference between a gross downward flux proportional to $\alpha_X \cdot pX$ and a gross upward flux proportional to $[X_{aq}]$. The upward and downward fluxes are independent (i.e., they do not impede each other). Thus, for CO_2, which exchanges O atoms upon contact with water, the dilution term is straightforward: it is equal to the gross downward flux $k_{CO_2} \cdot \alpha_{CO_2} \cdot pCO_2$, which can be used to calculate a maximum deposition velocity in the photochemical model (*SI Appendix*, Eq. S4). Thus, for CO_2, the dilution term is entirely independent of GPP. We explain how this is implemented in *Methods*.

For O_2, the situation is more complicated because isotopes are not exchanged unless the O_2 is taken up by respiration, so one cannot simply use the gross upward and downward fluxes implied by Eq. **11**. The relevant air–sea exchange flux should include only the O_2 that is reprocessed by respiration and photosynthesis. Furthermore, O_2 that is produced by photosynthesis within the surface ocean and then consumed in situ by respiration should not be counted as contributing to this exchange flux. An additional consideration is that the time-averaged net O_2 flux at the atmosphere–ocean interface must be approximately zero if the system is to remain in steady state. (We can neglect the ~10 Tmol · yr^{-1} of O_2 that is consumed by oxidative weathering on the continents [table 10.1 in ref. 54.]) Thus, the surface ocean must remain near Henry's Law equilibrium with the atmosphere on average according to Eq. **11**. However, in reality, the surface ocean departs substantially from equilibrium at different localities and at different seasons, driving measurable atmosphere–ocean O_2 exchange (55).

We can account for these complex O_2 exchange processes in our globally averaged model by following an approach pioneered by Bender et al. (52). On the modern Earth, marine GPP produces ~12,000 Tmol · O_2 · yr^{-1} (52), a value that falls nicely in between more recent estimates of 8,000 to 17,000 Tmol · yr^{-1} (56). We use the older values here because they have been used by other authors (25, 34, 35, 37), so one can compare with their results. Bender et al. (52) estimate that 12% of marine GPP is recycled internally within the surface ocean, so the relevant sea–air (or air–sea) flux of O_2 is 12,000 × 0.88 = 10,600 Tmol · O_2 · yr^{-1}.

To estimate the recycled O_2 fraction at lower pO_2 levels, one must understand the logic by which Bender et al. (52) calculated their 12% modern value. They compared the timescale for air–sea exchange of O_2 with that for uptake by respiration. The timescale for air–sea exchange is the dissolved O_2 reservoir size in the ocean mixed layer divided by the (gross) upward O_2 flux from Eq. **11**. Both quantities are proportional to pO_2 (at least on a time average), so the exchange timescale is just a constant equal to the depth of the ocean mixed layer divided by the piston velocity. The timescale for uptake by respiration is equal to the dissolved O_2 reservoir divided by GPP, so it depends linearly on pO_2 if GPP remains constant. Today, the timescale for air–sea exchange is ~1/14 that for respiration, so most photosynthetically generated O_2 escapes to the atmosphere. At lower O_2 levels, this ratio decreases, so more photosynthetic O_2 is recycled. The calculation is shown explicitly in *SI Appendix*, section 2.1.2. The results are shown in Fig. 1. Importantly, GPP is assumed to remain constant all the way down to 0.01 PAL O_2, thereby maximizing dilution of the $\Delta'^{17}O$ signal.

At pO_2 levels of 1% PAL and below, the O_2 exchange flux calculated by this method approaches the "piston velocity (*PV*) limit," so we simply use the latter value as we do for CO_2. Again, this maximizes the rate of air–sea O_2 transfer, and thus minimizes the $\Delta'^{17}O$ signal in O_2. The limiting O_2 flux, Φ_{PV}, is readily calculated by setting the dissolved O_2 concentration equal to zero in Eq. **11**: $\Phi_{PV} = k_{O_2} \cdot \alpha_{O_2} \cdot pO_2 \cong 6.5 \times (pO_2/1 \text{ bar})$ moles · m^{-2} · d^{-1}, using the O_2 solubility from *SI Appendix*, Table S1. Converting time units to years and multiplying by the area of the surface ocean, 5.1×10^{14} m^2, yields the *PV* limit values shown in *SI Appendix*, Table S3 and in Fig. 1. More details about model implementation are shown in *Methods*.

Critically, our estimated air–sea O_2 exchange fluxes at low pO_2 levels are only weakly connected to marine GPP. The exchange flux could be lower than calculated here if Proterozoic GPP was substantially lower than today, but it cannot be higher unless Proterozoic GPP was higher than today, and pO_2 was also relatively high. This same reasoning implies that the O-MIF data from sedimentary sulfates are largely independent of marine GPP. Thus, previous attempts to estimate Proterozoic GPP from such data (e.g., ref. 25) need to be rethought.

Recycling by the Terrestrial Biosphere. According to Farquhar et al. (57) and Bender et al. (52), modern terrestrial GPP is

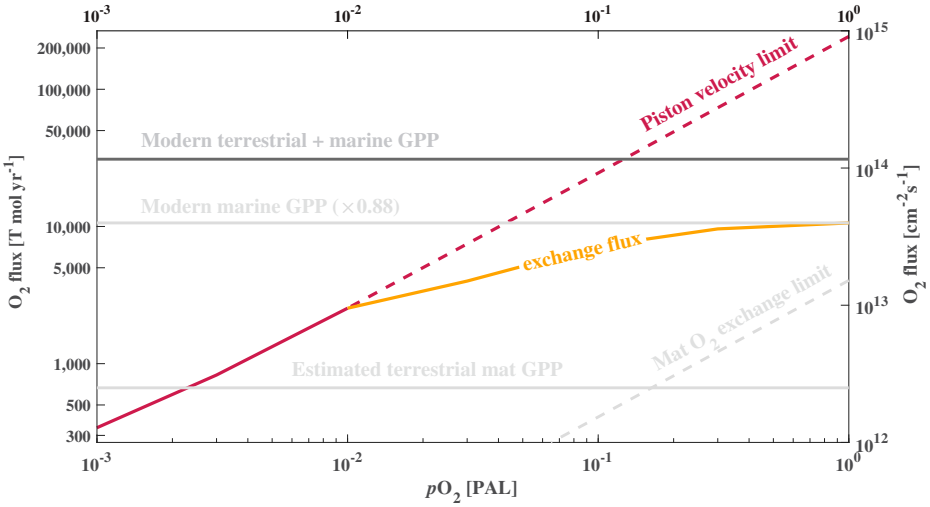

Fig. 1. Atmosphere–ocean O_2 exchange rates for different O_2 mixing ratios. The red curve represents the *PV* limit described in *Recycling by the Marine Biosphere*. The orange curve shows the calculated O_2 flux from *SI Appendix*, Table S3. The solid portions of the red and orange curves show the air–sea O_2 exchange rates employed in the low-O_2 calculations described in the text. The line labeled "Estimated terrestrial mat GPP" shows the effective O_2 exchange rate with the Proterozoic terrestrial biosphere in the Fig. 4*B* simulations. The dashed grey line is the effective *PV* for O_2 exchange between water-saturated mats and the atmosphere as described in *Recycling by the Terrestrial Biosphere*.

~14,100 Tmol · yr^{-1}. We again adopt values from Bender et al. (52), which remain close to more recent estimates: 12,250 Tmol · yr^{-1} (58) and 13,900 Tmol · yr^{-1} (59). However, photorespiration, which recycles O_2 without contributing to GPP, is also important. (In photorespiration, the enzyme RuBisCO oxygenates RuBP instead of carboxylating it, thereby short-circuiting the process of photosynthesis.) Thus, terrestrial uptake of O_2 rises to 20,400 Tmol · yr^{-1} when this process is considered (52). CO_2 is not produced by photorespiration, so the recycling of CO_2 by land plants should go at the slower, uncorrected GPP rate. Isotope exchange between CO_2 and plant water is complicated by the fact that the residence time of CO_2 in leaves is often shorter than the time scale (minutes) for CO_2 hydration. However, this problem is alleviated by the ubiquitous presence in plants of the enzyme carbonic anhydrase, which greatly accelerates hydration (51). Therefore, we assume that the $\Delta'^{17}O$ signal in CO_2 is almost zeroed out by this process as it is by recycling through the marine biosphere.

The processing of atmospheric O_2 by the terrestrial biosphere should have been slower during the mid-Proterozoic because vascular plants had not yet evolved. That said, significant portions of the exposed land surface may have been covered by microbial mats composed largely or partly of O_2-generating cyanobacteria (37, 60). Estimating the GPP of such mats is problematic because it is difficult to determine what fraction of the land surface should have been covered and because the area of the continents may have changed over time. Hence, we present calculations both with and without terrestrial mats. Based on a detailed study of a modern microbial mat in Indonesia, Finke et al. (60) estimated a terrestrial microbial mat GPP of 20 to 200 Tmol · O_2 · yr^{-1} for an Archean Earth with 1/6 the current land area. This translates to 120 to 1,200 Tmol · O_2 · yr^{-1} if the continents had grown to their present size by 1.4 Ga. Other authors have estimated Proterozoic microbial mat fluxes as high as 4,000 Tmol · O_2 · yr^{-1} (26). We use a terrestrial O_2 flux of 660 Tmol · yr^{-1} (~5% of modern terrestrial GPP) in the calculations discussed in the next paragraph and shown in Fig. 4B. This number is close to the mid-range terrestrial O_2 flux in Planavsky et al. (26).

Terrestrial microbial mats are subject to gas exchange constraints analogous to those imposed at the atmosphere–ocean interface. The surface of a water-saturated mat is much less permeable, though, than the turbulent ocean surface. Based on observations of the dissolved O_2 profile within a modern, water-saturated microbial mat by Finke et al. (60), we estimate that the effective *PV* for O_2 exchange between the mat and the atmosphere is about 1/60 that for atmosphere–ocean exchange (*SI Appendix*, section 2.2.8). The O_2 storage capacity for a mat is also much smaller than that of the surface ocean, so more of its photosynthetically produced O_2, ~70%, should be released to the atmosphere under low-pO_2 conditions (60). Because of the low exchange velocity, this O_2 could not have easily flowed back into the mat if pO_2 was low. Thus, to balance O_2 release, productive mats must also have released CH_4 (61) or H_2/CO (62) in stoichiometrically equivalent amounts; otherwise, that O_2 would have accumulated in the atmosphere. Here, we assume that the O_2 flux from mats was balanced by CH_4. The 660 Tmol(O_2) · yr^{-1} produced in our simulations that include mats corresponds to a CH_4 flux of 330 Tmol · yr^{-1}, or about 10 times the modern CH_4 flux (*SI Appendix*, section 1.3).

Results

Fits to Modern Earth. We implemented the chemistry and transport described in *Production of the O-MIF ($\Delta'^{17}O$) Signal during Ozone Formation* and *Dilution of the O-MIF Signal in O_2 and CO_2 via Biospheric Recycling* in a recent version of our one-dimensional photochemical (main) model (63), now linked to an isotopic model which duplicates this same chemistry for species containing one minor O isotope, either ^{17}O or ^{18}O. O_2 and CO_2 were treated as variables in both the main code and the isotopic code, but their boundary conditions were handled differently (see *Methods*). For our modern atmosphere calculations, the surface O_2 mixing ratio was set to 0.21 in the main code, and the CO_2 mixing ratio was set to 300 ppmv. We henceforth define these concentrations as 1 PAL. A relatively low value of pCO_2, near the preindustrial level of 280 ppmv, is appropriate for these calculations because the $\Delta'^{17}O$ signal in modern atmospheric O_2 has been gradually accumulating on a timescale commensurate with the lifetime of O_2 against isotopic recycling, ~1,200 y (35). In both the main code and the isotopic code, O_2 and CO_2 were given biospheric recycling fluxes using numbers from *Dilution of the O-MIF Signal in O_2 and CO_2 via*

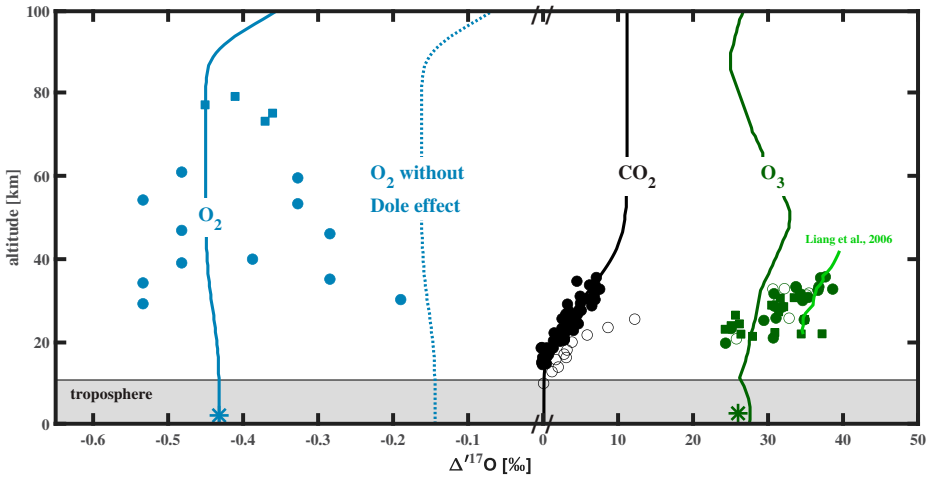

Fig. 2. Comparison between model-generated $\Delta'^{17}O$ values for our present-day simulation (curves) and atmospheric observations (symbols). Filled blue squares, blue circles, and the blue star are O_2 measurements for different altitudes from Pack et al. (67), Thiemens et al. (68), and Pack (27), respectively. The blue curves are model-predicted values with (solid) and without (dotted) corrections for the Dole effect. Measurements for CO_2 are from Kawagucci et al. (66), with filled black circles showing measurements from Kiruna, Sweden (68°N) on February 22, 1997, and open black circles showing measurements from Sanriku, Japan (39°N) on August 31, 1994. Measurements for O_3 are from Krankowsky et al. (49), with filled green circles, open green circles, and filled green squares showing measurements from Brazil, France, and Sweden, respectively. The green star is the measured surface fractionation of bulk O_3 from Vicars and Savarino (64). The light green curve shows the $\Delta'^{17}O$ of stratospheric O_3 calculated by Liang et al. (65). Note the scale change at $\Delta'^{17}O = 0‰$.

Biospheric Recycling. The O_2 flux from the combined marine and terrestrial biosphere was set equal to 31,000 Tmol · yr^{-1}. The CO_2 flux was 22,500 Tmol · yr^{-1}, which represents the sum of a gross marine flux calculated from the downward part of Eq. **11** along with a flux equal to terrestrial GPP.

Model predictions for $\Delta'^{17}O$ of O_2, O_3, and CO_2 are compared with measurements in Fig. 2. The stratospheric ozone measurements are from balloon flights carried out over the last ~40 y (see ref. 49 and references therein). They measure bulk ozone, separated cryogenically from air and converted quantitatively to O_2. Isotopic measurements of surface ozone were made indirectly by oxidizing nitrite and measuring the composition of the resulting nitrate (64). This measures only the transferrable (end atom) isotopic composition of O_3. Symmetric ozone (OQO) was assumed by those authors to have $\Delta'^{17}O = 0‰$. The fractionation values in the ozone data are affected by local meteorological factors such that the records from different places and times vary significantly. The shape of the modeled $\Delta'^{17}O$ profile for ozone reflects temperature- and pressure-dependent correction factors described in *SI Appendix*. The US 1976 Standard Atmosphere temperature profile was used in all calculations (*SI Appendix*, Fig. S7), including those at lower pO_2 levels. Sensitivity studies were performed to determine the effect on our results (*SI Appendix*, Fig. S7).

Importantly, to generate Fig. 2, the rate constant for the formation of asymmetric $^{49}O_3$ by reaction [**4**] has been adjusted downward by a factor β = 0.9772 (*SI Appendix*, Table S2).

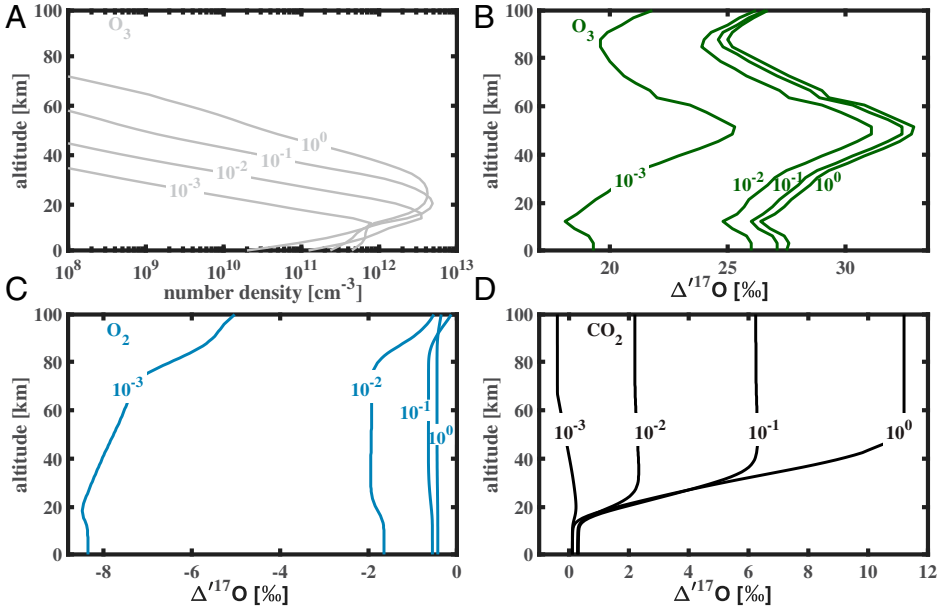

Fig. 3. Vertical profiles of (*A*) ozone (O_3) number density, (*B*) $\Delta'^{17}O$ of O_3, (*C*) $\Delta'^{17}O$ of O_2, and (*D*) $\Delta'^{17}O$ of CO_2 from photochemical model across a range of assumed ground-level atmospheric pO_2 values (in PAL). All results assume an atmospheric pCO_2 of 300 ppmv.

Without this correction factor, our model predicts $\Delta'^{17}O$ values of ~37‰ for O_3 at 25 km altitude, which is well above the average of the data. With the correction, $\Delta'^{17}O$ is ~28‰ at that altitude, which is within the range of observations; however, we underpredict $\Delta'^{17}O$ of O_3 above 30 km. The correction also brings us closer to the tropospheric ozone data (see Fig. 2). We feel justified in making this correction because we are ultimately interested in $\Delta'^{17}O$ of O_2, not O_3. Overpredicting the (positive) $\Delta'^{17}O$ of O_3 would cause us to also overpredict the magnitude of the (negative) $\Delta'^{17}O$ value of O_2. Young et al. (28) employed a similar strategy because their model also overpredicted $\Delta'^{17}O$ of O_3 and because they were also focused on O_2. The model of Liang et al. (65) overpredicted $\Delta'^{17}O$ of stratospheric O_3 as well (Fig. 2). Even with this correction factor, our model still slightly overpredicts $\Delta'^{17}O$ of surface ozone: we get ~27.5‰, whereas the reported value is ~26‰ (64). The actual value of $\Delta'^{17}O$ for surface ozone depends strongly on the $\Delta'^{17}O$ of symmetric O_3, which has not been measured experimentally. The discrepancy between calculation and measurement will only be resolved when we fully understand the isotopic fractionation in reactions [**4**–**6**].

Predicted $\Delta'^{17}O$ values for CO_2 increase from 0‰ at the surface to ~10‰ at 40 km, in agreement with the data from Sweden but not as close to the data from Japan (66). CO_2 is expected to be unfractionated near the surface because of rapid exchange of O isotopes with seawater. Comparisons of $\Delta'^{17}O$ between model and observations for H_2O_2 and nitrate are shown in *SI Appendix*, Fig. S1.

For O_2, the $\Delta'^{17}O$ value predicted near the surface by our model, −0.14‰, is well above observed values. The O_2 data are scattered, but Pack (27) suggests that −0.43‰ is a reasonable average value. This discrepancy is expected because according to Young et al. (28), 2/3 of the isotopic signal in modern O_2 is caused by the Dole effect, described in *Dilution of the O-MIF Signal in O_2 and CO_2 via Biospheric Recycling*. Accordingly, we subtract 0.29‰ from our calculated values to produce the solid curve in Fig. 2, which agrees well with the observations (27, 67, 68). Recall that this correction is expected to be smaller at lower pO_2 levels (*Dilution of the O-MIF Signal in O_2 and CO_2 via Biospheric Recycling*).

Results for Lower pO_2 Levels (Marine Biosphere Only). In a second set of calculations, we lowered atmospheric pO_2 from 1 to 10^{-3} PAL, keeping pCO_2 constant at 1 PAL. The interpretation of model results becomes complicated at $pO_2 < 10^{-3}$ PAL because terms other than air–sea exchange become important in the O_2 budget. In these simulations and in the ones described in the next section, we set the O_2 surface exchange flux equal to the values shown in *SI Appendix*, Table S3 using the *PV*-limited flux when pO_2 is lower than 0.03 PAL. Surface fluxes of other trace gases (CH_4, N_2O, CO, and H_2) were kept equal to their modern values (see *Methods*). The selected results are shown in Fig. 3. Notably, as O_2 decreases, the ozone layer moves downward, and its peak density decreases (Fig. 3*A*), consistent with earlier results (38, 69, 70).

Because the CO_2 mixing ratio is held constant in these calculations, the O_2:CO_2 ratio decreases at lower O_2 levels, causing O_2 to become more negatively fractionated (e.g., the $\Delta'^{17}O$ in surface O_2 is about −8.5‰ at 10^{-3} PAL pO_2) (Fig. 3*C*). This depletion in $\Delta'^{17}O$ in O_2 can be transferred to O_3, so the fractionation in ozone also decreases with decreasing O_2. For example, the surface ozone fractionation decreases from 27.5 to 19.3‰ as O_2 decreases from 1 to 10^{-3} PAL. Tropospheric CO_2 stays near 0‰ because isotopic exchange with seawater remains rapid in all these calculations. The large decrease in $\Delta'^{17}O$ for tropospheric O_2 at low O_2 levels is a result of mass balance. In today's atmosphere, the positive $\Delta'^{17}O$ signal in O_3 is transferred to CO_2 in the stratosphere as discussed in *Production of the O-MIF ($\Delta'^{17}O$) Signal during Ozone Formation*. CO_2 then flows downward into the troposphere and ultimately transfers that signal to seawater. Residual O_2 becomes negative in $\Delta'^{17}O$ as a result. However, at low pO_2, the ozone layer moves lower in the stratosphere or even into the troposphere (38, 70). CO_2 remains neutral or even slightly negative in $\Delta'^{17}O$ (Fig. 3*D*), while ozone transfers its positive $\Delta'^{17}O$ signal to water vapor— and from there to the ocean—by way of the

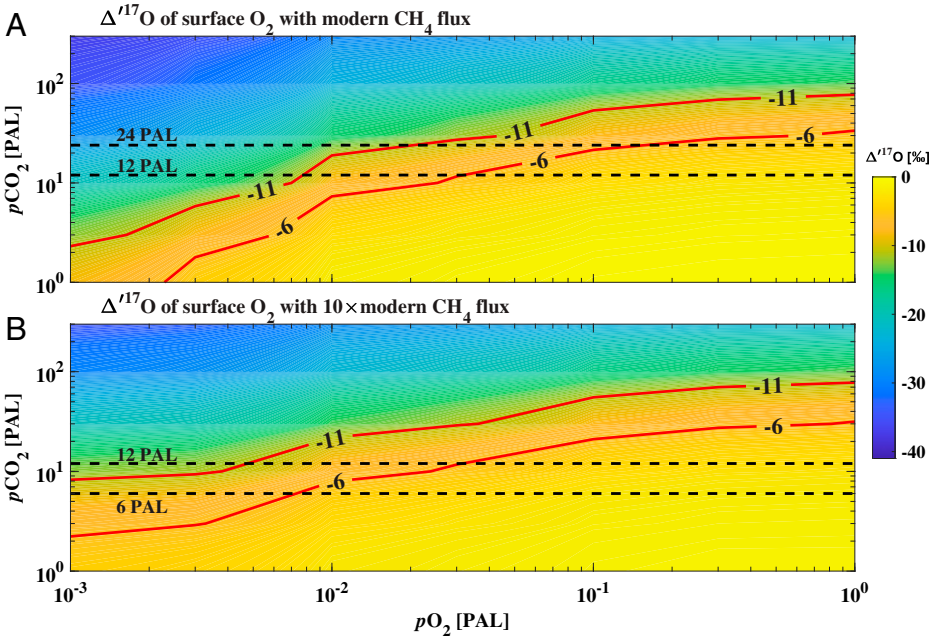

Fig. 4. Calculated $\Delta'^{17}O$ values for O_2 in the marine biosphere–only simulations (*A*) and the terrestrial biosphere–included simulations (*B*). The red-contoured interval represents the range of values that are consistent with the 1.4-Ga Sibley sulfate data, assuming 8 to 15% incorporation of O_2. The dashed lines represent various suggested constraints on pCO_2 discussed in the text.

HO_x chemistry described in *SI Appendix*, section 2.2.5. This latter process is highly efficient, and the atmospheric O_2 reservoir is small, so O_2 becomes strongly negative in $\Delta'^{17}O$.

Next, we repeated our calculations over a grid with pO_2 ranging from 1 to 10^{-3} PAL and with pCO_2 from 1 to 300 PAL, yielding 42 assumed pO_2/pCO_2 combinations. Following the methodology described earlier in this section and in *Methods*, CO_2 surface exchange fluxes remain at the *PV* limit, so they become large at high pCO_2 values. The O_2 exchange fluxes were taken from *SI Appendix*, Table S3. The calculated $\Delta'^{17}O$ values for ground-level O_2 are shown in Fig. 4*A*. Some authors (e.g., ref. 31) have suggested that the main oxidizing agent for pyrite is H_2O_2, not O_2. The $\Delta'^{17}O$ value of H_2O_2 tracks that of O_2 closely (*SI Appendix*, Fig. S4), however, suggesting that it may not matter which species actually causes the oxidation.

When pyrite is oxidized to sulfate by O_2, only 8 to 15% of the oxygen in the sulfate comes from O_2; the rest comes from water (71). By contrast, Killingsworth et al. (72) suggest that the incorporated O_2 fraction is 18 ± 9%. We use the lower numbers from Balci et al. (71) here to remain consistent with previous studies (25, 37). Higher O_2 incorporation in sulfate would lead to higher predicted pO_2 values. The 1.4-Ga Sibley sulfates were deposited in a shallow evaporative setting (25). The most negative $\Delta'^{17}O$ value observed in these sediments is −0.9‰. Indeed, all these data are below −0.3‰, below the range of Phanerozoic sulfates (25). The O_2 needed to produce this fractionation must therefore have $\Delta'^{17}O$ values in the range of −6 to −11‰. Most of this O_2 is taken up in the last oxidation step going from sulfite to sulfate (71), so we assume that a similar uptake fraction would apply to H_2O_2 (*SI Appendix*, Fig. S4). This range is represented by the red-contoured interval in Fig. 4*A*. The $\Delta'^{17}O$ values higher than −6‰ in O_2 are excluded by the Sibley data, assuming that the Balci et al. (71) oxidant incorporation factors are correct. The $\Delta'^{17}O$ values lower than −11‰ in O_2 cannot be excluded, but they would require bacterial reprocessing of dissolved sulfate and consequent dilution of the O-MIF signal within the water column beneath which the sulfates were deposited. We ignore the Dole effect correction to $\Delta'^{17}O$ of O_2 at pO_2 levels below 1 PAL. More than half of this correction comes from the terrestrial biosphere, which should have been greatly diminished at 1.4 Ga if pO_2 was low (*Recycling by the Terrestrial Biosphere*). Any Dole effect caused by the marine biosphere at that time would push our calculated $\Delta'^{17}O$ values lower for O_2, causing our predicted pO_2 values to be higher than those estimated in this section.

Not surprisingly, predicted $\Delta'^{17}O$ values for O_2 depend on both pO_2 and pCO_2. Thus, estimating pO_2 from Proterozoic data depends on having an accurate estimate for pCO_2. Unfortunately, constraints on pCO_2 span an order of magnitude. A credible lower limit on pCO_2 can be inferred from climate considerations, but the upper limit on pCO_2 is unclear. The two dashed horizontal lines in Fig. 4*A* indicate a range of plausible pCO_2 levels. The lower line is at ∼12 PAL (3,550 ppmv), and the upper line is at ∼24 PAL (7,100 ppmv). These estimates come from three-dimensional climate model simulations (73). According to their (zero-CH_4) climate model results, 3,550 ppmv CO_2 at 1.42 Ga would have produced a glacial climate with a mean surface temperature of 10.7 °C, whereas 7,100 ppmv CO_2 would have produced a mean surface temperature of 18.6 °C—sufficient to keep the continents (but not the poles) ice free. These calculations account for the fact that solar luminosity at that time was ∼90% of the present value (74).

If one considers these values to be lower and upper bounds on pCO_2 and assumes no dilution of the O-MIF signal, pO_2 should be in the range of 0.8 to 20% PAL (Fig. 4*A*). These values are roughly an order of magnitude higher than the 0.1 to 1% PAL values estimated by Planavsky et al. (37) from these same data. Part of the difference is attributable to the more detailed photochemical model used here and to our improved treatment of air–sea gas exchange. However, much of it stems from our more restricted range of plausible pCO_2 values. Planavsky et al. (37) assumed a range of pCO_2 values randomly distributed between 2 and 500 PAL, along with a substantial terrestrial oxygen flux. If we allow pCO_2 values as low as 2 PAL, our predicted pO_2 could be 0.1% PAL or even lower. These low CO_2 levels would have resulted in global glaciation unless Earth's greenhouse effect at that time was supplemented by large amounts of CH_4 and/or N_2O (73, 75). However, N_2O photolyzes rapidly below ∼0.1 PAL O_2, so its greenhouse contribution should have been modest (63, 76). CH_4 is a more likely Proterozoic greenhouse gas; its possible effect is considered in the following section.

A weakness in the above argument is that Liu et al. (73) considered their 24 PAL pCO_2 estimate to be a lower limit for mid-Proterozoic pCO_2 (assuming no methane), not an upper limit. The climate record suggests that the "Boring Billion" period between 1.8 to 0.8 Ga was ice free, except for a few possible exceptions. Glaciations have been reported in the King Leopold formation in northwestern Australia at 1.8 Ga (77) and in the Vazante Group in Brazil, which was once considered Neoproterozoic in age but which has been redated at 1.1 to 1.3 Ga (78). Atmospheric CO_2 levels above ∼30 PAL would permit pO_2 values as high as today, according to Fig. 4*A*. Thus, other arguments are needed to place an upper limit on pCO_2 if we wish to constrain mid-Proterozoic pO_2 levels.

Additional Results for Lower pO_2 Levels (Terrestrial Biosphere Included). Finally, we repeated the calculations shown in Fig. 4*A* but with a terrestrial (microbial mat) biosphere included. Terrestrial GPP was set at 660 Tmol $(O_2) \cdot yr^{-1}$ with an accompanying CH_4 flux equal to half that value (see *Recycling by the Terrestrial Biosphere*). We assumed O_2 exchange rates with the marine biosphere were the same as in *Results for Lower pO_2 Levels (Marine Biosphere Only)* . The effect on $\Delta'^{17}O$ of O_2 is shown in Fig. 4*B*. The red contours at −6 and −11‰ shift upwards, particularly at low pO_2 levels where air–sea O_2 exchange is slow. Most of this change is caused by higher rates of O_2 recycling, which dilutes the O-MIF signal.

However, the interpretation of these results is changed even more if one considers the effect of higher CH_4 levels on climate. The high CH_4 flux assumed here, 10 times the modern value, causes atmospheric CH_4 to increase from 1.6 ppmv in the base, 1 PAL O_2 model to as much as 60 ppmv at some O_2 levels (*SI Appendix*, Fig. S5). The nonlinear response of CH_4 concentration to its surface input rate has been seen in other models [e.g., Pavlov et al. (79)]. Even at low pO_2, the calculated CH_4 mixing ratio is 15 to 20 ppmv, enough to generate 2 to 3° C of greenhouse warming (76). One CO_2 doubling produces roughly this same temperature increase when the climate is relatively warm; consequently, we reduced the lower pCO_2 limit in Fig. 4*B* from 12 to 6 PAL. When this change is made, the permissible range for pO_2 extends all the way down to 0.1% PAL or lower. If the CO_2 level and CH_4 flux assumed here are correct for the mid-Proterozoic, few constraints can be placed on pO_2 from the existing O-MIF data. Terrestrial GPP values of 4,000 Tmol $\cdot$ yr^{-1} or higher (26) can be ruled out, though, because they produce $\Delta'^{17}O$ values in O_2 less negative than −6‰ (*SI Appendix*, Fig. S6).

Discussion

Geologic Constraints on Mid-Proterozoic pCO_2. Past atmospheric CO_2 concentrations can be inferred from geologic data as well as from climate models (54). One approach is to study the composition of ancient soils preserved as paleosols. The two samples that are closest in time to the period of interest are the

Flin Flon paleosol at 1.8 Ga (80) and the Sturgeon Falls paleosol at 1.1 Ga (81). The original authors used the fact that these paleosols retained iron during weathering to derive estimates for pO_2. Sheldon (82) reanalyzed them for pCO_2 using a similar kinetic approach. Interpolating between his (very high) pCO_2 value at 1.8 Ga and his much lower value at 1.1 Ga yielded a pCO_2 of 3,600 ppmv (12 PAL in our units) at 1.4 Ga (82). This value should be considered as a lower limit, as Sheldon's analysis method assumes that all the CO_2 that enters the soil reacts with silicate minerals. A reanalysis of earlier Archean paleosols by Kanzaki and Murakami (83) using a different methodology yields pCO_2 values that are 10 to 20 times higher than those calculated by Sheldon for those same samples. Thus, the paleosol data support the lower limit on pCO_2 shown in Fig. 4*A* but may not provide a useful upper limit.

Our lower limit on mid-Proterozoic pCO_2 is also supported by a study of the carbon isotopic composition of microfossils preserved in the Ruyang Group in Shanxi Province, China (84). Carbon isotope fractionation decreases when CO_2 is less available; hence, the highly depleted $\delta^{13}C$ values (-32 to $-36‰$) measured in the microfossils require relatively high pCO_2. They estimate a lower limit of 3,600 ppmv (12 PAL) at 1.4 Ga, similar to Sheldon's estimate from paleosols.

Upper limits on mid-Proterozoic pCO_2 have been estimated by looking at fossil cyanobacteria as well as their effect on the nature of the sedimentary record. Riding (85) argued that a decline in pCO_2 below 10,000 ppmv (33 PAL) at ∼1,400 to 1,300 Ma resulted in blooms of planktic cyanobacteria that induced "whitings" of carbonate mud in the water column whose sedimentary accumulation began to dominate carbonate platforms at that time. A later study of cyanobacterial sheath calcification suggests that 3,600 ppmv (12 PAL) is an upper limit on pCO_2 at 1.2 Ga (86). These authors argue that falling CO_2 levels led to the evolution of intracellular carbon-concentrating mechanisms that pumped CO_2 into cell carboxysomes, raising the pH of the surrounding cytosol and triggering in vivo carbonate deposition.

We conclude that atmospheric pCO_2 was likely falling during the mid-Proterozoic and that concentrations of 12 to 24 PAL at 1.4 Ga are in the right ballpark based on geologic proxy data. If so, then the very low pO_2 levels allowed by Fig. 4*B* may not be supported. Moving the lower limit on pCO_2 back to 12 PAL in Fig. 4*B* would imply a lower limit of ∼0.5% PAL for pO_2. However, even this limit would not be firm because of possible dilution of the O-MIF signal during sulfate precipitation in the water column.

Additional Thoughts on Mid-Proterozoic CH_4. Our results depend critically on the concentration of atmospheric CH_4. When CH_4 is low, that is, when the biogenic methane flux is comparable to (or lower than) today, we can derive a lower limit on mid-Proterozoic pO_2, ∼0.8% PAL, from the Sibley data if we assume no recycling of the O-MIF signal in the water column (*Results for Lower pO_2 Levels (Marine Biosphere Only)*). At 10 times the current methane flux, we get no lower limit on pO_2 whatsoever (*Additional Results for Lower pO_2 Levels (Terrestrial Biosphere Included)*). In the latter calculations, we assumed a substantial methane flux from terrestrial microbial mats. This assumption is speculative for two reasons: 1) The fractional land coverage and productivity of such mats during the mid-Proterozoic is uncertain. 2) Whether mats grown under low pO_2 could actually generate this much methane is unclear. The cultivation of mats under such conditions might help to answer the latter question.

Some authors (e.g., ref. 79) have also suggested that methane could have been generated in significant amounts in Proterozoic marine sediments. Their argument was that, if GPP was relatively high and the recycling of organic matter by aerobic decay and sulfate reduction were both low, more of the organic matter should have been recycled by fermentation and methanogenesis. This argument has been criticized by other researchers (87–89) who argue that methane production in sediments remains low even under low-O_2, low-sulfate conditions, partly because of the fact that biological productivity must have been lower because of slower recycling of critical nutrients such as phosphorus (88, 89). Unless this objection can be countered, we accept that marine methane production must have been low.

Conclusions

We provide a more mechanistically grounded framework for interpreting the triple oxygen isotope record through Earth's history. Our model improves on the treatment of atmospheric ozone photochemistry and introduces key constraints on air–sea gas exchange. The O-MIF record provides a measure of the atmospheric ratio of O_2:CO_2, not of pO_2 itself. A reasonable lower limit on pCO_2 at 1.4 Ga, ∼3,600 ppmv or 12 PAL, can be estimated from climate models and is supported by geochemical proxy data. CO_2 partial pressures lower than this value can be tolerated climatically but only if CH_4 concentrations were high (>15 ppmv). Given $pCO_2 \geq 12$ PAL and low CH_4, mid-Proterozoic O_2 should have been >0.8% PAL if the Sibley data are taken at face value. The dilution of the $\Delta'^{17}O$ signal by the reprocessing of sulfate within the water column above where the sulfates were deposited could decrease this lower limit on pO_2, but there is no easy way to quantify this effect. High CH_4 and lower pCO_2 would also allow pO_2 to have been lower.

Upper limits on pO_2 during the mid-Proterozoic are difficult to estimate from the O-MIF data, again because of uncertainties in pCO_2. Marine GPP cannot be estimated reliably from sedimentary O-MIF data because of complications imposed by constraints on air–sea gas transfer. Terrestrial microbial mat GPP is constrained by similar considerations. If atmospheric pO_2 was low, then terrestrial GPP could only have been high if mats emitted large quantities of CH_4 or H_2/CO to the atmosphere to soak up the emitted O_2. Despite all these limitations, the sedimentary O-MIF record remains a useful tool for investigating the composition of the Precambrian atmosphere. If better proxies for pCO_2 can be obtained, along with more direct measures of $\Delta'^{17}O$ of atmospheric O_2, the O-MIF record may eventually lead to a quantitative understanding of the history of atmospheric O_2.

Methods

Our photochemical model includes a main model for normal chemical reactions and an isotopic model designed for oxygen isotope reactions. The main model is derived from Stanton et al. (63). It extends from the ground up to 100 km in altitude and contains full atmospheric chemistry for CHONS (carbon, hydrogen, oxygen, nitrogen, and sulfur) species (up through C_1 for carbon). Chlorine chemistry has been removed from the model, as it is less important for the preindustrial atmosphere than for today. The main model includes 42 species linked by 175 chemical reactions (*SI Appendix*). Boundary conditions for the long-lived species are described later in this section. The main model is run to steady state, assuming a fixed solar zenith angle and using a fully implicit time integration scheme.

The boundary conditions in the model are critical and must be chosen carefully. At the upper boundary (100 km), most species are given an effusion velocity of zero (equivalent to zero flux). Major species (O_2 and CO_2) that are rapidly photodissociated above this level are allowed to flow up, whereas their photolysis products (CO and O) flow down in stoichiometric ratios. The lower boundary condition for each long-lived species can be either fixed mixing ratio, fixed flux, or fixed deposition velocity. O_2 and CO_2 are always assigned fixed mixing ratios in the main model. They serve as control variables in our calculations. Most other long-lived species are assigned constant deposition velocities following Kasting et al. (90). In the modern atmosphere simulation, some biogenic or partly biogenic trace gases (CH_4, N_2O, H_2, and CO) are

given mixing ratios equal to their observed values (*SI Appendix*, section 2.1.1). The main model then calculates surface fluxes needed to sustain them. At lower pO_2 levels, these fluxes are held constant in both the main and isotopic models. For CH_4, the modern mixing ratio is fixed at 1.6 ppmv; this yields a corresponding upward flux of 33 Tmol $\cdot$ yr^{-1}, which is comparable to estimates for the CH_4 flux on modern Earth (91). In the calculations that include terrestrial microbial mats (*Additional Results for Lower pO_2 Levels (Terrestrial Biosphere Included)*), the CH_4 flux was increased to 330 Tmol $\cdot$ yr^{-1}, balancing the assumed mat O_2 flux.

The key to calculating the dilution of the O-MIF signal by biospheric recycling is to give special treatment to O_2 and CO_2. Unlike shorter-lived gases such as CH_4, their surface mixing ratios do not depend in a simple way on their surface fluxes. The surface fluxes calculated by the photochemical model, given fixed mixing ratio boundary conditions, are tiny compared to the recycling fluxes described in *Dilution of the O-MIF Signal in O_2 and CO_2 via Biospheric Recycling*. Moreover, in the (globally averaged) photochemical model, each gas must be flowing either up or down at the lower boundary, whereas, on the real Earth, O_2 and CO_2 are flowing both upward and downward in different places and at different times of the year. We simulate this exchange by inserting fictitious tropospheric chemical production terms for O_2 and CO_2 equal to their calculated recycling fluxes (*SI Appendix*, Table S3) in both main and isotopic codes. These sources are distributed evenly between 0 and 11 km, as should be appropriate for a long-lived gas injected into a rapidly mixed reservoir. The injected O_2 and CO_2 have nowhere to go except down through the lower boundary. Dividing those downward fluxes by the number density of each gas yields a deposition velocity, which is then saved for use in the isotopic code. For $pO_2 \leq 1\%$ PAL, to ensure that we maximize the rate of O_2 exchange, we gradually increase the fictitious production term until the calculated O_2 deposition velocity is equal to the *PV* described in *Recycling by the Marine Biosphere* (also see *SI Appendix*, Table S9).

The structure of the isotopic model is like that of the main model but with significant deviations in the chemical scheme and boundary conditions. The isotopic model contains 358 reactions that duplicate the chemistry in the main model but for isotopically substituted species (*SI Appendix*, Tables S5 and S8). Both minor O isotopes, ^{18}O and ^{17}O, are represented in the isotopic model by a single parameter, Q. Q is assumed to be sufficiently scarce so that species containing a Q atom never react with each other; hence, one never produces doubly substituted isotopic species. This is a good assumption for both ^{18}O (~0.2% of total oxygen) and ^{17}O (~0.04%). The isotope routine is run twice for each calculation, once for ^{17}O and once for ^{18}O. The $\delta^{x}O$ values found in this manner are combined to calculate $\Delta'^{17}O$ by Eq. **1**. Species in the isotopic model are initialized with values proportional to their concentrations in the main code. Those species containing one O atom are set equal to their main model counterpart, species containing two O atoms are set equal to twice their main model values, and so on. This ensures that each isotopically substituted species starts out with zero fractionation (because the isotopic composition of the species is related to the number of Q atoms [one] divided by the total number of O atoms in the molecule).

The boundary conditions for the species in the isotopic model are the same as in the main model except for O_2 and CO_2 (*SI Appendix*, Table S9). Instead of assuming fixed mixing ratios, we use fixed deposition velocities for OQ and COQ. Each gas is given the same deposition velocity as that derived in the main code, along with the same distributed tropospheric recycling flux. Thus, their surface concentrations can now change in response to fractionating chemistry that occurs within the atmosphere. Because they start close to the solution, the isotopic equations can be iterated to steady state using Newton's method. *SI Appendix*, Table S9 shows the boundary conditions used in the main/isotope codes and a flowchart of the model operation described in this section. Further details on the methodology are provided in *SI Appendix*.

Data Availability. All model output data and code are available on Zenodo with the identifier https://doi.org/10.5281/zenodo.4609694.

ACKNOWLEDGMENTS. We thank Kristie A. Boering for her contributions during the development phase of this project, especially for guiding the comparison with modern atmospheric data. We also thank Christof Janssen for insightful guidance on the chemical kinetics of ozone isotope formation. P.L. was supported by the National Natural Science Foundation of China (Grants 41888101, 42105043, 42121005 and 91958214) and China Postdoctoral Science Foundation (Grants 2021M690142 and 2021T140629). Funding for this project was also provided by The Pennsylvania State University, the China Scholarship Council, and Yale University.

1. L. R. Kump, The rise of atmospheric oxygen. *Nature* **451**, 277–278 (2008).
2. T. W. Lyons, C. T. Reinhard, N. J. Planavsky, The rise of oxygen in Earth's early ocean and atmosphere. *Nature* **506**, 307–315 (2014).
3. J. F. Kasting, Earth's early atmosphere. *Science* **259**, 920–926 (1993).
4. H. D. Holland, The oxygenation of the atmosphere and oceans. *Philos. Trans. R. Soc. Lond. B Biol. Sci.* **361**, 903–915 (2006).
5. J. Farquhar, H. Bao, M. Thiemens, Atmospheric influence of Earth's earliest sulfur cycle. *Science* **289**, 756–759 (2000).
6. G. Luo *et al.*, Rapid oxygenation of Earth's atmosphere 2.33 billion years ago. *Sci. Adv.* **2**, e1600134 (2016).
7. A. A. Pavlov, J. F. Kasting, Mass-independent fractionation of sulfur isotopes in Archean sediments: Strong evidence for an anoxic Archean atmosphere. *Astrobiology* **2**, 27–41 (2002).
8. L. J. Alcott, B. J. W. Mills, S. W. Poulton, Stepwise Earth oxygenation is an inherent property of global biogeochemical cycling. *Science* **366**, 1333–1337 (2019).
9. G. Shields-Zhou, L. Och, The case for a Neoproterozoic oxygenation event: Geochemical evidence and biological consequences. *GSA Today* **21**, 4–11 (2011).
10. D. E. Canfield, A new model for Proterozoic ocean chemistry. *Nature* **396**, 450–453 (1998).
11. D. B. Cole *et al.*, A shale-hosted Cr isotope record of low atmospheric oxygen during the Proterozoic. *Geology* **44**, 555–558 (2016).
12. N. J. Planavsky *et al.*, Earth history. Low mid-Proterozoic atmospheric oxygen levels and the delayed rise of animals. *Science* **346**, 635–638 (2014).
13. D. Tang, X. Shi, X. Wang, G. Jiang, Extremely low oxygen concentration in mid-Proterozoic shallow seawaters. *Precambrian Res.* **276**, 145–157 (2016).
14. E. J. Bellefroid *et al.*, Constraints on Paleoproterozoic atmospheric oxygen levels. *Proc. Natl. Acad. Sci. U.S.A.* **115**, 8104–8109 (2018).
15. N. J. Planavsky *et al.*, A case for low atmospheric oxygen levels during Earth's middle history. *Emerg. Top. Life Sci.* **2**, 149–159 (2018).
16. S. Zhang *et al.*, Sufficient oxygen for animal respiration 1,400 million years ago. *Proc. Natl. Acad. Sci. U.S.A.* **113**, 1731–1736 (2016).
17. D. E. Canfield *et al.*, Highly fractionated chromium isotopes in Mesoproterozoic-aged shales and atmospheric oxygen. *Nat. Commun.* **9**, 2871 (2018).
18. R. R. Large *et al.*, Atmosphere oxygen cycling through the Proterozoic and Phanerozoic. *Miner. Depos.* **54**, 485–506 (2019).
19. A. Liu *et al.*, Mesoproterozoic oxygenated deep seawater recorded by early diagenetic carbonate concretions from the Member IV of the Xiamaling Formation, North China. *Precambrian Res.* **341**, 105667 (2020).
20. X.-M. Liu *et al.*, A persistently low level of atmospheric oxygen in Earth's middle age. *Nat. Commun.* **12**, 351 (2021).
21. D. B. Cole *et al.*, On the co-evolution of surface oxygen levels and animals. *Geobiology* **18**, 260–281 (2020).
22. D. B. Mills, D. E. Canfield, Oxygen and animal evolution: Did a rise of atmospheric oxygen "trigger" the origin of animals? *BioEssays* **36**, 1145–1155 (2014).
23. D. B. Mills *et al.*, Oxygen requirements of the earliest animals. *Proc. Natl. Acad. Sci. U.S.A.* **111**, 4168–4172 (2014).
24. A. D. Anbar, A. H. Knoll, Proterozoic ocean chemistry and evolution: A bioinorganic bridge? *Science* **297**, 1137–1142 (2002).
25. P. W. Crockford *et al.*, Triple oxygen isotope evidence for limited mid-Proterozoic primary productivity. *Nature* **559**, 613–616 (2018).
26. N. J. Planavsky *et al.*, Evolution of the structure and impact of Earth's biosphere. *Nature Reviews Earth & Environment* **2**, 123–139 (2021).
27. A. Pack, Isotopic traces of atmospheric O_2 in rocks, minerals, and melts. *Rev. Mineral. Geochem.* **86**, 217–240 (2021).
28. E. D. Young, L. Y. Yeung, I. E. Kohl, On the $\Delta^{17}O$ budget of atmospheric O_2. *Geochim. Cosmochim. Acta* **135**, 102–125 (2014).
29. H. Bao *et al.*, Anomalous ^{17}O compositions in massive sulphate deposits on the Earth. *Nature* **406**, 176–178 (2000).
30. P. W. Crockford *et al.*, Claypool continued: Extending the isotopic record of sedimentary sulfate. *Chem. Geol.* **513**, 200–225 (2019).
31. J. D. Hemingway *et al.*, Triple oxygen isotope insight into terrestrial pyrite oxidation. *Proc. Natl. Acad. Sci. U.S.A.* **117**, 7650–7657 (2020).
32. B. R. Cowie, D. T. Johnston, High-precision measurement and standard calibration of triple oxygen isotopic compositions ($\delta^{18}O$, $\Delta'^{17}O$) of sulfate by F2 laser fluorination. *Chem. Geol.* **440**, 50–59 (2016).
33. Z. D. Sharp, J. A. Wostbrock, Standardization for the triple oxygen isotope system: Waters, silicates, carbonates, air, and sulfates. *Rev. Mineral. Geochem.* **86**, 179–196 (2021).
34. X. Cao, H. Bao, Dynamic model constraints on oxygen-17 depletion in atmospheric O_2 after a snowball Earth. *Proc. Natl. Acad. Sci. U.S.A.* **110**, 14546–14550 (2013).
35. B. Luz, E. Barkan, M. L. Bender, M. H. Thiemens, K. A. Boering, Triple-isotope composition of atmospheric oxygen as a tracer of biosphere productivity. *Nature* **400**, 547–550 (1999).
36. M. S. W. Hodgskiss, P. W. Crockford, Y. Peng, B. A. Wing, T. J. Horner, A productivity collapse to end Earth's Great Oxidation. *Proc. Natl. Acad. Sci. U.S.A.* **116**, 17207–17212 (2019).

37. N. J. Planavsky, C. T. Reinhard, T. T. Isson, K. Ozaki, P. W. Crockford, Large mass-independent oxygen isotope fractionations in mid-Proterozoic sediments: Evidence for a low-oxygen atmosphere? *Astrobiology* **20**, 628–636 (2020).
38. A. Segura *et al.*, Ozone concentrations and ultraviolet fluxes on Earth-like planets around other stars. *Astrobiology* **3**, 689–708 (2003).
39. J. E. Heidenreich III, M. H. Thiemens, A non-mass-dependent isotope effect in the production of ozone from molecular oxygen. *J. Chem. Phys.* **78**, 892–895 (1983).
40. C. Janssen, J. Guenther, K. Mauersberger, D. Krankowsky, Kinetic origin of the ozone isotope effect: A critical analysis of enrichments and rate coefficients. *Phys. Chem. Chem. Phys.* **3**, 4718–4721 (2001).
41. S. Anderson, D. Hülsebusch, K. Mauersberger, Surprising rate coefficients for four isotopic variants of $O+O_2+M$. *J. Chem. Phys.* **107**, 5385–5392 (1997).
42. Y. Q. Gao, R. A. Marcus, Strange and unconventional isotope effects in ozone formation. *Science* **293**, 259–263 (2001).
43. A. Teplukhin, D. Babikov, Several levels of theory for description of isotope effects in ozone: Symmetry effect and mass effect. *J. Phys. Chem. A* **122**, 9177–9190 (2018).
44. A. Teplukhin, I. Gayday, D. Babikov, Several levels of theory for description of isotope effects in ozone: Effect of resonance lifetimes and channel couplings. *J. Chem. Phys.* **149**, 164302 (2018).
45. C. Janssen, J. Guenther, D. Krankowsky, K. Mauersberger, Temperature dependence of ozone rate coefficients and isotopologue fractionation in ^{16}O-^{18}O oxygen mixtures. *Chem. Phys. Lett.* **367**, 34–38 (2003).
46. J. Guenther, B. Erbacher, D. Krankowsky, K. Mauersberger, Pressure dependence of two relative ozone formation rate coefficients. *Chem. Phys. Lett.* **306**, 209–213 (1999).
47. K. Mauersberger, Measurement of heavy ozone in the stratosphere. *Geophys. Res. Lett.* **8**, 935–937 (1981).
48. K. Mauersberger, Ozone isotope measurements in the stratosphere. *Geophys. Res. Lett.* **14**, 80–83 (1987).
49. D. Krankowsky *et al.*, Stratospheric ozone isotope fractionations derived from collected samples. *J. Geophys. Res. D Atmospheres* **112**, D08301 (2007).
50. Y. L. Yung, A. Y. Lee, F. W. Irion, W. B. DeMore, J. Wen, Carbon dioxide in the atmosphere: Isotopic exchange with ozone and its use as a tracer in the middle atmosphere. *J. Geophys. Res.* **102**, 10857–10866 (1997).
51. P. Ciais *et al.*, A three-dimensional synthesis study of $\delta^{18}O$ in atmospheric CO_2: 1. Surface fluxes. *J. Geophys. Res. D Atmospheres* **102**, 5857–5872 (1997).
52. M. Bender, T. Sowers, L. Labeyrie, The Dole effect and its variations during the last 130,000 years as measured in the Vostok ice core. *Global Biogeochem. Cycles* **8**, 363–376 (1994).
53. R. Wanninkhof, Relationship between wind speed and gas exchange over the ocean revisited. *Limnol. Oceanogr. Methods* **12**, 351–362 (2014).
54. D. C. Catling, J. F. Kasting, *Atmospheric Evolution on Inhabited and Lifeless Worlds* (Cambridge University Press, 2017).
55. R. F. Keeling, S. R. Shertz, Seasonal and interannual variations in atmospheric oxygen and implications for the global carbon cycle. *Nature* **358**, 723–727 (1992).
56. M. C. Carvalho, K. G. Schulz, B. D. Eyre, Respiration of new and old carbon in the surface ocean: Implications for estimates of global oceanic gross primary productivity. *Global Biogeochem. Cycles* **31**, 975–984 (2017).
57. G. D. Farquhar *et al.*, Vegetation effects on the isotope composition of oxygen in atmospheric CO_2. *Nature* **363**, 439–443 (1993).
58. G. Badgley, L. D. L. Anderegg, J. A. Berry, C. B. Field, Terrestrial gross primary production: Using NIR_V to scale from site to globe. *Glob. Change Biol.* **25**, 3731–3740 (2019).
59. A. J. Norton *et al.*, Estimating global gross primary productivity using chlorophyll fluorescence and a data assimilation system with the BETHY-SCOPE model. *Biogeosciences* **16**, 3069–3093 (2019).
60. N. Finke *et al.*, Mesophilic microorganisms build terrestrial mats analogous to Precambrian microbial jungles. *Nat. Commun.* **10**, 4323 (2019).
61. M. Zhao, C. T. Reinhard, N. Planavsky, Terrestrial methane fluxes and Proterozoic climate. *Geology* **46**, 139–142 (2018).
62. T. M. Hoehler, B. M. Bebout, D. J. Des Marais, The role of microbial mats in the production of reduced gases on the early Earth. *Nature* **412**, 324–327 (2001).
63. C. L. Stanton *et al.*, Nitrous oxide from chemodenitrification: A possible missing link in the Proterozoic greenhouse and the evolution of aerobic respiration. *Geobiology* **16**, 597–609 (2018).
64. W. C. Vicars, J. Savarino, Quantitative constraints on the ^{17}O-excess ($\Delta^{17}O$) signature of surface ozone: Ambient measurements from 50°N to 50°S using the nitrite-coated filter technique. *Geochim. Cosmochim. Acta* **135**, 270–287 (2014).
65. M. C. Liang *et al.*, Isotopic composition of stratospheric ozone. *J. Geophys. Res. D Atmospheres* **111**, D02302 (2006).
66. S. Kawagucci *et al.*, Long-term observation of mass-independent oxygen isotope anomaly in stratospheric CO_2. *Atmos. Chem. Phys.* **8**, 6189–6197 (2008).
67. A. Pack *et al.*, Tracing the oxygen isotope composition of the upper Earth's atmosphere using cosmic spherules. *Nat. Commun.* **8**, 15702 (2017).
68. M. H. Thiemens, T. Jackson, E. C. Zipf, P. W. Erdman, C. van Egmond, Carbon dioxide and oxygen isotope anomalies in the mesosphere and stratosphere. *Science* **270**, 969–972 (1995).
69. J. S. Levine, P. B. Hays, J. C. Walker, The evolution and variability of atmospheric ozone over geological time. *Icarus* **39**, 295–309 (1979).
70. J. F. Kasting, T. Donahue, The evolution of atmospheric ozone. *J. Geophys. Res. Oceans* **85**, 3255–3263 (1980).
71. N. Balci, W. C. Shanks III, B. Mayer, K. W. Mandernack, Oxygen and sulfur isotope systematics of sulfate produced by bacterial and abiotic oxidation of pyrite. *Geochim. Cosmochim. Acta* **71**, 3796–3811 (2007).
72. B. A. Killingsworth, H. Bao, I. E. Kohl, Assessing pyrite-derived sulfate in the Mississippi River with four years of sulfur and triple-oxygen isotope data. *Environ. Sci. Technol.* **52**, 6126–6136 (2018).
73. P. Liu, Y. Liu, Y. Hu, J. Yang, S. A. Pisarevsky, Warm climate in the "Boring Billion" era. *Acta Geologica Sinica-English Edition* **93**, 40–43 (2019).
74. J. N. Bahcall, M. Pinsonneault, S. Basu, Solar models: Current epoch and time dependences, neutrinos, and helioseismological properties. *Astrophys. J.* **555**, 990–1012 (2001).
75. R. P. Fiorella, N. D. Sheldon, Equable end Mesoproterozoic climate in the absence of high CO_2. *Geology* **45**, 231–234 (2017).
76. A. L. Roberson, J. Roadt, I. Halevy, J. F. Kasting, Greenhouse warming by nitrous oxide and methane in the Proterozoic Eon. *Geobiology* **9**, 313–320 (2011).
77. P. W. Schmidt, G. E. Williams, Palaeomagnetism of red beds from the Kimberley Group, Western Australia: Implications for the palaeogeography of the 1.8 Ga King Leopold glaciation. *Precambrian Res.* **167**, 267–280 (2008).
78. N. J. Geboy *et al.*, Re–Os age constraints and new observations of Proterozoic glacial deposits in the Vazante Group, Brazil. *Precambrian Res.* **238**, 199–213 (2013).
79. A. A. Pavlov, M. T. Hurtgen, J. F. Kasting, M. A. Arthur, Methane-rich Proterozoic atmosphere? *Geology* **31**, 87–90 (2003).
80. H. D. Holland, C. R. Feakes, E. A. Zbinden, The Flin Flon paleosol and the composition of the atmosphere 1.8 BYBP. *Am. J. Sci.* **289**, 362–389 (1989).
81. E. A. Zbinden, H. D. Holland, C. R. Feakes, S. Dobos, The Sturgeon Falls paleosol and the composition of the atmosphere 1.1 Ga BP. *Precambrian Res.* **42**, 141–163 (1988).
82. N. D. Sheldon, Precambrian paleosols and atmospheric CO_2 levels. *Precambrian Res.* **147**, 148–155 (2006).
83. Y. Kanzaki, T. Murakami, Estimates of atmospheric CO_2 in the Neoarchean–Paleoproterozoic from paleosols. *Geochim. Cosmochim. Acta* **159**, 190–219 (2015).
84. A. J. Kaufman, S. Xiao, High CO_2 levels in the Proterozoic atmosphere estimated from analyses of individual microfossils. *Nature* **425**, 279–282 (2003).
85. R. Riding, Cyanobacterial calcification, carbon dioxide concentrating mechanisms, and Proterozoic–Cambrian changes in atmospheric composition. *Geobiology* **4**, 299–316 (2006).
86. L. C. Kah, R. Riding, Mesoproterozoic carbon dioxide levels inferred from calcified cyanobacteria. *Geology* **35**, 799–802 (2007).
87. S. L. Olson, C. T. Reinhard, T. W. Lyons, Limited role for methane in the mid-Proterozoic greenhouse. *Proc. Natl. Acad. Sci. U.S.A.* **113**, 11447–11452 (2016).
88. T. A. Laakso, D. P. Schrag, Methane in the Precambrian atmosphere. *Earth Planet. Sci. Lett.* **522**, 48–54 (2019).
89. T. A. Laakso, D. P. Schrag, A small marine biosphere in the Proterozoic. *Geobiology* **17**, 161–171 (2019).
90. J. F. Kasting, H. D. Holland, J. P. Pinto, Oxidant abundances in rainwater and the evolution of atmospheric oxygen. *J. Geophys. Res.* **90**, 10497–10510 (1985).
91. S. Kirschke *et al.*, Three decades of global methane sources and sinks. *Nat. Geosci.* **6**, 813–823 (2013).